Full paper

Grain-boundary-resistance-less $Na_3SbS_{4-x}Se_x$ solid electrolytes for all-solid-state sodium batteries

Hongli Wan[a,b], Jean Pierre Mwizerwa[a,b], Fudong Han[c], Wei Weng[a,b], Jing Yang[a], Chunsheng Wang[c,*], Xiayin Yao[a,b,**]

[a] Ningbo Institute of Materials Technology and Engineering, Chinese Academy of Sciences, 315201, Ningbo, PR China
[b] Center of Materials Science and Optoelectronics Engineering, University of Chinese Academy of Sciences, Beijing, 100049, PR China
[c] Department of Chemical and Biomolecular Engineering, University of Maryland, College Park, MD, 20742, United States

ABSTRACT

A nanoscaled $Na_3SbS_{3.75}Se_{0.25}$ solid electrolyte with less grain-boundary resistance was synthesized using a liquid/solid fusion technology. The $Na_3SbS_{3.75}Se_{0.25}$ solid electrolyte shows a high ionic conductivity of $4.03 \times 10^{-3} \, S \, cm^{-1}$ at room temperature due to the significantly decreased amorphous phase in the electrolyte. Moreover, the small particle size of the solid electrolytes enhances the contact between solid electrolyte and electrode, reducing the interfacial contact resistance. As a result, $FeS_2/Na_3SbS_{3.75}Se_{0.25}/Na$ all-solid-state sodium batteries achieve a high specific capacity of $140.6 \, mAh \, g^{-1}$ for 300 cycles at a high current of $500 \, mA \, g^{-1}$. In addition, $FeS_2/Na_3SbS_{3.75}Se_{0.25}/Na$ cells also demonstrate a high rate-capacity of 365.3, 301.8, 210.1 and $96.0 \, mAh \, g^{-1}$ at current densities of 50, 300, 500 and $1000 \, mA \, g^{-1}$, respectively. The liquid/solid fusion technology is a unique synthesis strategy to develop superionic electrolytes for room temperature all-solid-state sodium secondary battery.

1. Introduction

The high-temperature sodium sulfur battery faces inherent safety concerns due to the molten sodium anode and sulfur cathode at high operating temperatures of 300 °C–350 °C [1,2]. Extensive researches have been devoted to reduce the operation temperature of all-solid-state sodium ion battery to room temperature [3–7]. The solid-state sodium ion conductive electrolytes for room temperature sodium battery have to meet the following stringent requirements: (1) high ionic conductivity of $10^{-4} \, S \, cm^{-1}$, (2) excellent compatibility to the cathodes with a low interfacial resistance, and (3) superb stability against metal sodium. However, all current solid Na-ion electrolytes, including oxide electrolytes, polymer electrolytes and sulfide electrolytes, cannot satisfy all these requirements. Although sintered dense oxide electrolytes exhibits a high ionic conductivity [8], the large interfacial resistance between oxide electrolyte and cathode material limits the power density [9]. Adding polymer into oxide electrolytes can reduce the interfacial resistance of oxide electrolyte [10,11]. However, the inherent disadvantages of polymer electrolyte with a narrow electrochemical window and poor oxidation resistivity [10] still restrict the high voltage cathodes or/and Na metal anodes.

Sulfide electrolytes [3,12–18] have captured much attention due to their high ionic conductivity, low particle-boundary resistance by densification of electrolyte pellet through a simple cold press. Moreover, their excellent ductility can effectively ameliorate the volume changes of active material in electrodes to maintain sufficient electrolyte/active material contact, leading to improved cyclic stability and high rate capability of the battery. Significant advances in enhancing the ionic conductivity of sulfide electrolytes have been achieved. Several high Na-ion conductive electrolytes such as Na_3PS_4 $(2.0 \times 10^{-4} \, S \, cm^{-1})$ [12], $94Na_3PS_4 \cdot 6Na_4SiS_4$ $(7.4 \times 10^{-4} \, S \, cm^{-1})$ [19], Na_3PSe_4 $(1.16 \times 10^{-3} \, S \, cm^{-1})$ [14], Na_3SbS_4 $(1.1 \times 10^{-3} \, S \, cm^{-1})$ [3,13] and $Na_{11}Sn_2PS_{12}$ $(1.4 \times 10^{-3} \, S \, cm^{-1})$ [20] have been reported. Clearly, the ionic conductivity of these solid Na-ion electrolytes is still lower than that of lithium ion electrolytes. To further enhance the ionic conductivity of the sulfide electrolytes, the P and S elements in Na_3PS_4 electrolyte were replaced by ions with large size to increase the Na^+ migration channel and reduce interaction between the mobile ions and structural anions [3,14]. The ionic conductivities of Na_3PSe_4 electrolytes $(1.16 \times 10^{-3} \, S \, cm^{-1})$ and Na_3SbS_4 $(3.0 \times 10^{-3} \, S \, cm^{-1})$ are much higher than that of Na_3PS_4 $(2.0 \times 10^{-4} \, S \, cm^{-1})$ because the radius of Se and Sb is larger than that

of S and P, respectively. Simultaneous substitution of P by Sb and S by Se in Na_3PS_4 can further enhance the ionic conductivity of $Na_3SbS_{4-x}Se_x$. With a high grain ionic conductivity, the ionic conductivity at grain boundary and particle-to-particle boundary in cold-press electrolyte membrane becomes a limiting step for ionic transport in electrolytes. The electrolyte with less grain-boundary resistance will have a high ionic conductivity. The particle size of the electrolytes may slightly increase the ionic conduction resistance, but it will significantly reduce the contact resistance at electrolyte/electrode, which limits the performance of the all-solid-state battery [16,21]. In all-solid-state battery, the contacts between electrolyte and electrode material are point to point due to the immobility of the components [22]. Although the sulfide electrolytes synthesized by solid-state reaction have higher ductility than oxide electrolytes, the contact resistance between sulfide electrolyte and cathode materials is still high after cold pressing. Minimizing the particle size of the electrolytes can increase the interfacial contact to cathode and form a uniform ionic conduction network, thus reducing the contact resistance with cathodes.

Liquid-phase reaction can effectively reduce the particle size and tune morphology of the sulfide electrolytes [16,17,21,23,24]. However, the ionic conductivity of the electrolyte synthesized using a liquid-phase reaction is generally one order of magnitude lower than that of the electrolyte synthesized using a solid-state reaction method due to the presence of large amorphous phase between grains. To achieve a high ionic conductivity of nano-sized electrolyte, the conductivity of solid electrolytes (grain and grain boundary) should be maximized, which is very challenged for both liquid-phase reaction method and solid-sate reaction method.

In this work, we developed nano-sized super conductive $Na_3SbS_{3.75}Se_{0.25}$ electrolyte by simultaneous substitution of P by Sb and S by Se in Na_3PS_4 using a liquid-solid fusion synthesis technology, which combines the merits of small particle size from liquid-phase reaction and high ionic conductivity from solid-phase reaction. The $Na_3SbS_{3.75}Se_{0.25}$ electrolyte with tetragonal phase and particle size of 200–500 nm shows a high ionic conductivity of $4.03 \times 10^{-3}\,S\,cm^{-1}$. By coupling FeS_2 cathode and Na anodes, the $FeS_2/Na_3SbS_{3.75}Se_{0.25}/Na$ all-solid-state sodium batteries exhibit a high discharge capacity of 140.6 mAh g^{-1} at 500 mA g^{-1} after 300 cycles and superior rate capability with specific capacities of 365.3, 301.8, 210.1 and 96.0 mAh g^{-1} at current densities of 50, 300, 500 and 1000 mA g^{-1}, respectively.

2. Experimental section

Preparation of $Na_3SbS_{4-x}Se_x$ electrolytes and FeS_2 cathode materials: $Na_3SbS_{4-x}Se_x$ solid electrolytes were synthesized using a liquid/solid fusion technology. Typically, Na_2S (95%, Aladdin Chemistry Co., Ltd), Sb_2S_3 (99.9%, Aladdin Chemistry Co., Ltd), S (99.9%, Aladdin Chemistry Co., Ltd) and Se (99%, Aladdin Chemistry Co., Ltd) with a mole ratio of 3:1:(2-2x):2x were added in acetonitrile (99.8%, Aladdin Chemistry Co., Ltd), and stirred at 50 °C for 24 h. After the complete reaction, the precursor solution was distilled in vacuum and then dried at 80 °C for 12 h to remove the residual solvent. The obtained powders were then ball-milled using a planetary ball mill apparatus (Retch, PM400) at a fixed rotation speed of 500 rpm for 13.5 h. Finally, the obtained powders were annealed at 450 °C under argon atmosphere to get the $Na_3SbS_{4-x}Se_x$ electrolytes (LS-$Na_3SbS_{4-x}Se_x$). For comparison, the $Na_3SbS_{4-x}Se_x$ electrolytes were also synthesized using solid-state reaction (S-$Na_3SbS_{4-x}Se_x$) or liquid-phase reaction (L-$Na_3SbS_{4-x}Se_x$). S-$Na_3SbS_{4-x}Se_x$ electrolytes were prepared by mechanical milling of stoichiometric mixture of Na_2S, Sb_2S_3 and S for 13.5 h, followed by heat treatment at 450 °C. L-$Na_3SbS_{4-x}Se_x$ precursors were synthesized by mixing Na_2S, Sb_2S_3 and S in acetonitrile as mentioned above, and then annealed at 450 °C to obtain L-$Na_3SbS_{4-x}Se_x$ electrolytes without ball-milling before annealing. Therefore, the L-$Na_3SbS_{4-x}Se_x$ electrolyte was prepared by liquid-phase reaction followed by heat-treatment, S-$Na_3SbS_{4-x}Se_x$ electrolyte was prepared by ball-milling procedure

followed by heat-treatment, LS-$Na_3SbS_{4-x}Se_x$ electrolyte was obtained through liquid-phase reaction, followed by ball-milling and then an annealing process.

The detailed synthesis procedures of pyrite FeS_2 microsphere cathode material can be found from our previous published work [17].

Characterizations: X-ray powder diffraction (XRD) was performed using Bruker D8 Advance Diffractometer with Cu K_α radiation ($\lambda = 1.54178$ Å) at a voltage of 40 kV and a current of 40 mA. Morphology of the electrolytes was investigated by a scanning electron microscope (SEM, S-4800, Hitachi), and the microstructures of the electrolytes were determined by a high-resolution transmission electron microscopy (HRTEM, FEI Tecnai G^2 F20). The electrolyte composition and elemental distribution were obtained by energy dispersive spectroscopy (EDS) and scanning transmission electron microscopy (STEM).

Electrochemical performance measurements: The ionic conductivities of the $Na_3SbS_{4-x}Se_x$ electrolytes were measured under argon atmosphere by electrochemical impedance spectroscopy (EIS) at frequency range from 1 MHz to 10 Hz with the amplitude of 15 mV using a Solartron 1470E multi-channel potentiostat electrochemical workstation (Solartron Public Co., Ltd.). During impedance tests, carbon paste was used as blocking electrode. To assemble all-solid-state $FeS_2/$ $Na_3SbS_{3.75}Se_{0.25}/Na$ sodium batteries, 100 mg of $Na_3SbS_{3.75}Se_{0.25}$ electrolyte was first pressed into solid electrolyte layer under 240 MPa, then, the hand mixed FeS_2 - $Na_3SbS_{3.75}Se_{0.25}$ - Super P composite powders with a weight ratio of 4: 5: 1 ($\sim 1.5\,mg\,cm^{-2}$) were uniformly spread on one side of $Na_3SbS_{3.75}Se_{0.25}$ electrolyte layer and pressed under 240 MPa. Finally, the sodium foil was attached on the other side of $Na_3SbS_{3.75}Se_{0.25}$ electrolyte layer and pressed under 360 MPa to form an all-solid-state full cell. All the cell fabrication processes were performed in an argon-filled glove box. Electrochemical tests were measured at different current densities in the cut-off voltage of 0.9–2.7 V in room temperature under an argon atmosphere using multichannel battery test system (LAND CT-2001A, Wuhan Rambo Testing Equipment Co., Ltd.). The specific discharge/charge capacities were calculated based on the mass of FeS_2. Cyclic voltammetry (CV) curves of $FeS_2/Na_3SbS_{3.75}Se_{0.25}/Na$ all-solid-state sodium batteries were tested on the aforementioned electrochemical workstation in the potential range of 0.9–2.7 V.

3. Results and discussion

$Na_3SbS_{4-x}Se_x$ ($x = 0$, 0.25, 0.5, 0.75) electrolytes with different Se substitution were synthesized using three method: liquid phase reaction (denoted as L-$Na_3SbS_{4-x}Se_x$), solid state reaction (S-$Na_3SbS_{4-x}Se_x$), and liquid-solid fusion reaction (LS-$Na_3SbS_{4-x}Se_x$). Briefly, in the liquid phase reaction method, the raw materials Na_2S, Sb_2S_3 and S were mixed in acetonitrile to form electrolyte precursor solution, and then dried precursor solution at 80 °C for 12 h followed by annealing at 450 °C to obtain $Na_3SbS_{4-x}Se_x$ electrolyte powders. Solid-phase method synthesized electrolytes (S-$Na_3SbS_{4-x}Se_x$) were prepared by mechanical milling of stoichiometric mixture of Na_2S, Sb_2S_3 and S for 13.5 h, followed by heat treatment at 450 °C. The LS-$Na_3SbS_{4-x}Se_x$ is synthesized by ball-milled the L-$Na_3SbS_{4-x}Se_x$ precursor powders and then annealed at 450 °C under argon atmosphere to get the $Na_3SbS_{4-x}Se_x$ electrolytes.

Fig. 1a shows the XRD pattern of L-$Na_3SbS_{4-x}Se_x$ ($x = 0$, 0.25, 0.5, 0.75). For $x = 0$, all the diffraction peaks of pure Na_3SbS_4 could be indexed to the cubic structure. The characteristic diffraction peaks at $2\theta = 17.48°$, 24.82°, 30.51°, 35.38°, 39.72°, 43.70°, 47.40°, 54.23°, and 57.43° correspond to the diffraction from the (1 1 0), (2 0 0), (2 1 1), (2 2 0), (3 1 0), (2 2 2), (3 2 1), (4 1 1) and (4 2 0) planes of cubic structure, respectively. For $x = 0.25$ and 0.5 electrolytes, the diffraction peaks shift to a lower angle because the replacement of the S^{2-} anions by the larger Se^{2-} anion induces a volume expansion. Further increasing the Se content to 0.75, Se and some unknown phases appear. The impedance spectra of L-$Na_3SbS_{4-x}Se_x$ with different Se substitution is shown in Fig. 1b. The L-$Na_3SbS_{3.75}Se_{0.25}$ electrolytes achieve the
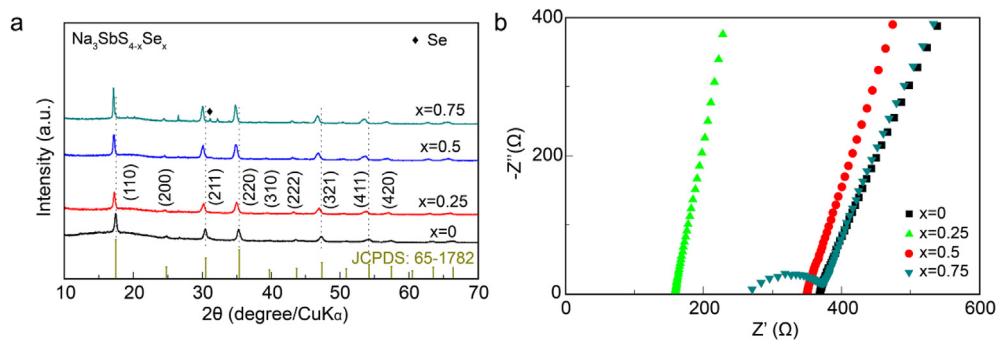
Fig. 1. (a) XRD patterns and (b) Impedance spectra of $Na_3SbS_{4-x}Se_x$ electrolytes.

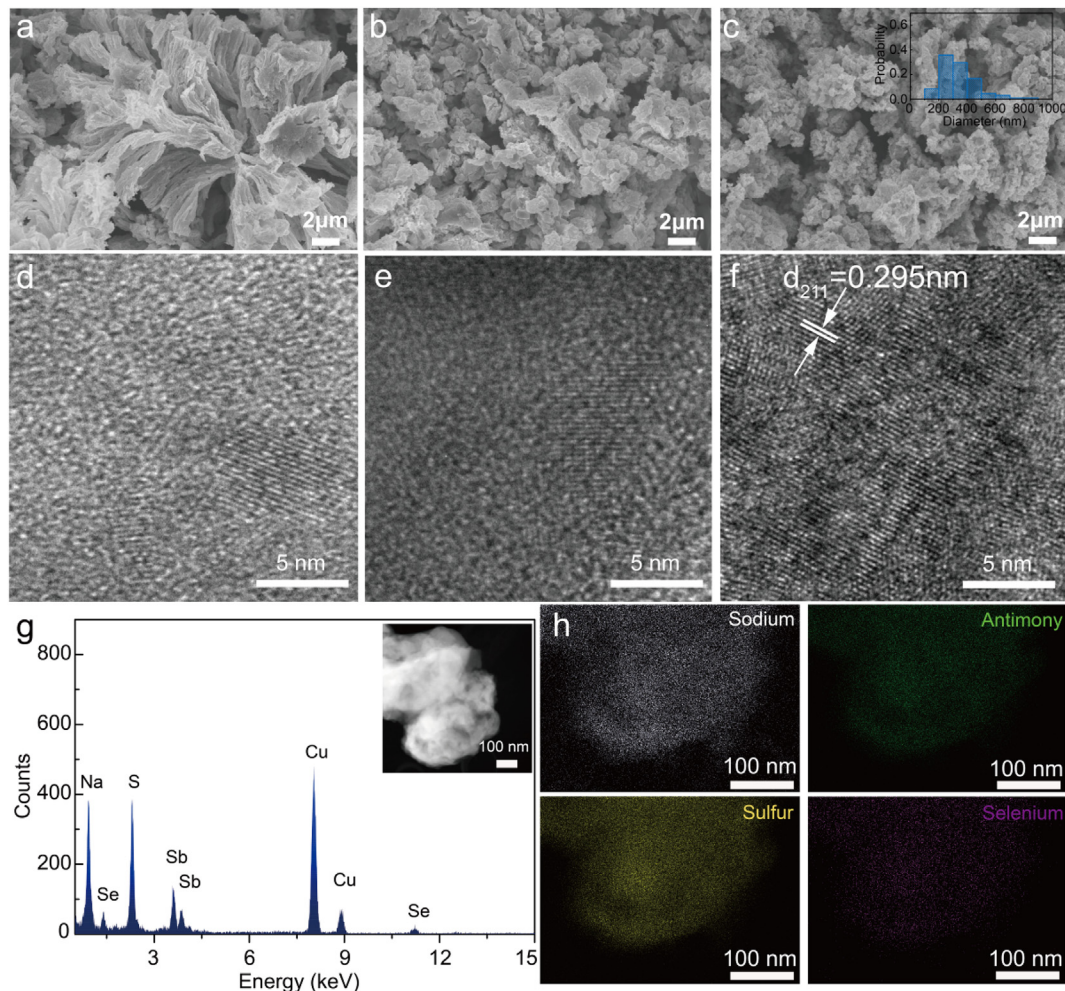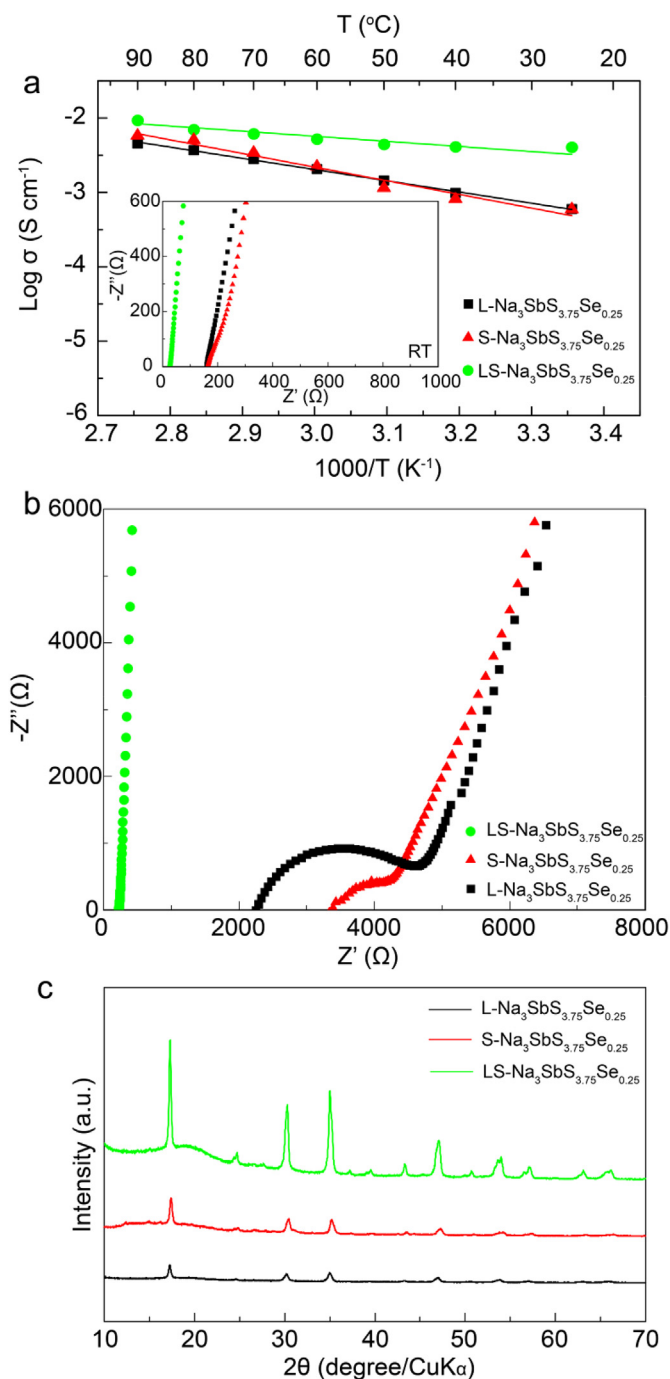**Fig. 2.** SEM images of $Na_3SbS_{3.75}Se_{0.25}$ electrolytes synthesized by (a) liquid-phase method, (b) solid-phase method and (c) liquid/solid fusion technology (the inset is the statistical particle size distribution of the electrolytes). HRTEM image of $Na_3SbS_{3.75}Se_{0.25}$ electrolytes synthesized by (d) liquid-phase method, (e) solid-phase method and (f) liquid/solid fusion technology. (g) EDS spectra (element Cu belongs to copper grid for TEM test) and (h) STEM images of $Na_3SbS_{3.75}Se_{0.25}$ electrolytes synthesized liquid/solid fusion technology.

highest ionic conductivity of $5.98 \times 10^{-4}\,S\,cm^{-1}$ in all $Na_3SbS_{4-x}Se_x$ ($x = 0$, 0.25, 0.5, 0.75) electrolytes, which is more than two times higher than that of pure Na_3SbS_4 ($2.52 \times 10^{-4}\,S\,cm^{-1}$) electrolytes. The high ionic conductivity of L-$Na_3SbS_{3.75}Se_{0.25}$ is because the expansion of the crystal volume by substitution of S with Se facilitates the diffusion of Na^+. However, when the Se substitution increases to $x = 0.75$, impurities precipitated in Na_3SbS_4 electrolytes reduces the ionic conductivity to $2.45 \times 10^{-4}\,S\,cm^{-1}$ as evidenced by a large grain boundary semicircle in the high frequency. $Na_3SbS_{3.75}Se_{0.25}$ with $x = 0.25$ was selected as optimized electrolytes to be synthesized using

other two methods (solid-phase reaction and liquid-solid fusion reaction) to reduce the particle size and grain boundary resistance.

Fig. 2a–c shows the morphology of the $Na_3SbS_{3.75}Se_{0.25}$ electrolytes synthesized using three different methods: liquid-phase method, solid-phase method and liquid/solid fusion technology. The L-$Na_3SbS_{3.75}Se_{0.25}$ electrolyte consists of nanofibers cluster with seaweed morphology (Fig. 2a), while the S-$Na_3SbS_{3.75}Se_{0.25}$ electrolytes shows irregular particles with a wider size distribution (Fig. 2b). The LS-$Na_3SbS_{3.75}Se_{0.25}$ electrolyte displays a much small and uniform particle size of about 200–500 nm (Fig. 2c). The uniform nanoscaled particle

Fig. 3. (a) Arrhenius conductivity plots of $Na_3SbS_{3.75}Se_{0.25}$ electrolytes. (The inset displays the impedance spectra of $Na_3SbS_{3.75}Se_{0.25}$ electrolytes at room temperature). (b) The impedance spectra of $Na_3SbS_{3.75}Se_{0.25}$ electrolyte at 233 K. (c) XRD patterns of $Na_3SbS_{3.75}Se_{0.25}$ electrolytes synthesized by different methods.

size can reduce the electrode/electrolyte interface resistance after cold pressing process [25]. The crystal structure of the LS-$Na_3SbS_{3.75}Se_{0.25}$ electrolytes were revealed using HRTEM. As shown in Fig. 2f, a clear lattice with interplanar distance of 0.295 nm is observed, which attributes to the (2 1 1) lattice plane of tetragonal structured $Na_3SbS_{3.75}Se_{0.25}$ [3]. The LS-$Na_3SbS_{3.75}Se_{0.25}$ grains are connected by grain boundary with fast ion conduction, while a large amount of amorphous structure between grains are observed in L-$Na_3SbS_{3.75}Se_{0.25}$ and S- $Na_3SbS_{3.75}Se_{0.25}$ (Fig. 2d and e). The EDS spectrum in Fig. 2g reflects that the obtained electrolytes contain element sodium,

antimony, sulfur and selenium. Besides, the STEM image (Fig. 2h) for a single LS-$Na_3SbS_{3.75}Se_{0.25}$ particle reveals that all of the component elements are homogenously distributed throughout the electrolytes.

The LS-$Na_3SbS_{3.75}Se_{0.25}$ electrolyte synthesized using liquid/solid fusion technology has a high ionic conductivity of $4.03 \times 10^{-3} \, S \, cm^{-1}$ at room temperature (inset EIS in Fig. 3a). The calculated activation energy ($21.73 \, kJ \, mol^{-1}$) of LS-$Na_3SbS_{3.75}Se_{0.25}$ electrolytes (Fig. 3a) is much lower than that of L-$Na_3SbS_{3.75}Se_{0.25}$ ($28.89 \, kJ \, mol^{-1}$) and S-$Na_3SbS_{3.75}Se_{0.25}$ ($31.14 \, kJ \, mol^{-1}$) electrolytes. To identify the role of grain boundary in ionic conductivity, the EISs of L-$Na_3SbS_{3.75}Se_{0.25}$, S-$Na_3SbS_{3.75}Se_{0.25}$ and LS-$Na_3SbS_{3.75}Se_{0.25}$ electrolytes were measured at $-40 \, °C$ because grain boundary resistance only appear at a low-temperature [26]. As shown in Fig. 3b, the EIS of L-$Na_3SbS_{3.75}Se_{0.25}$ electrolyte shows a largest grain boundary resistance at $-40 \, °C$ because the amorphous phase with a low ionic conductivity forms at grain boundary [27]. By contrast, no grain boundary resistance is observed in EIS of LS-$Na_3SbS_{3.75}Se_{0.25}$ electrolyte and the bulk resistance is also much lower than that of L-$Na_3SbS_{3.75}Se_{0.25}$ and S-$Na_3SbS_{3.75}Se_{0.25}$ electrolytes because the milling process transforms the amorphous phase and less-conductive crystal cubic-phase in L-$Na_3SbS_{3.75}Se_{0.25}$ to high conductive tetragonal-phase structure, and simultaneously decreases the particle size of the electrolyte, and thus improving the ionic conductivity of $Na_3SbS_{3.75}Se_{0.25}$ electrolyte. The structure difference of $Na_3SbS_{3.75}Se_{0.25}$ electrolytes synthesized by different methods was confirmed by XRD (Fig. 3c). After ball-milling, cubic-phase in L-$Na_3SbS_{3.75}Se_{0.25}$ transfers to tetragonal-phase in LS-$Na_3SbS_{3.75}Se_{0.25}$ electrolyte. Besides, the LS-$Na_3SbS_{3.75}Se_{0.25}$ electrolytes have a higher peak intensity than that of L-$Na_3SbS_{3.75}Se_{0.25}$ and S-$Na_3SbS_{3.75}Se_{0.25}$ electrolytes because of the enhanced crystallization. The highly conductive grain boundary with negligible grain boundary resistance reduces the resistance of the battery that fabricated through a simple cold-pressing [25].

The electrochemical performance of the $Na_3SbS_{3.75}Se_{0.25}$ electrolytes was evaluated in an all-solid-state sodium battery using pyrite FeS_2 as a cathode and Na as an anode. Fig. 4a–c shows the CV curves of $FeS_2/Na_3SbS_{3.75}Se_{0.25}/Na$ all-solid-state sodium battery. A clear reduction peak at 1.6 V and corresponding oxidation peak at 2.2 V after first cycles are observed in all three $FeS_2/L-Na_3SbS_{3.75}Se_{0.25}/Na$ and $FeS_2/S-Na_3SbS_{3.75}Se_{0.25}/Na$ and $FeS_2/LS-Na_3SbS_{3.75}Se_{0.25}/Na$ cells due to the insertion/extraction of Na^+ into Na_xFeS_2. The low reduction peak at 1.1 V in the first cycle in three $FeS_2/Na_3SbS_{3.75}Se_{0.25}/Na$ cells is associated with the formation of Na_2FeS_2. In the first anodic scan, a broad oxidation peak at about 2.2 V is observed, due to the extraction of Na^+ from the Na_2FeS_2 and the formation of Na_xFeS_2 [28,29]. The CV curves in the following two cycles are similar in all of the batteries, implying an identical reaction occurs as follows: $(y-x) \, Na^+ + (y-x) \, e^- + Na_xFeS_2 \leftrightarrow Na_yFeS_2$ $(0 < x < 2, x < y)$. However, the redox peak currents at 1.6 and 2.2 V in $FeS_2/LS-Na_3SbS_{3.75}Se_{0.25}/Na$ cell are much larger than these in $FeS_2/L-Na_3SbS_{3.75}Se_{0.25}/Na$ and $FeS_2/S-Na_3SbS_{3.75}Se_{0.25}/Na$ cells, demonstrating a fast reaction kinetic in $FeS_2/LS-Na_3SbS_{3.75}Se_{0.25}/Na$ cells. The high reaction kinetic also evidenced by smallest peak separation between the reduction and oxidation in $FeS_2/LS-Na_3SbS_{3.75}Se_{0.25}/Na$ cell among these three type batteries, due to the higher ionic conductivity of LS-$Na_3SbS_{3.75}Se_{0.25}$ and the enhanced solid-solid contact at $FeS_2/LS-Na_3SbS_{3.75}Se_{0.25}$ interface. Fig. 4d–f shows the galvanostatic discharge/charge profiles of three $FeS_2/Na_3SbS_{3.75}Se_{0.25}/Na$ all-solid-state sodium batteries at a cut-off voltage of 0.9–2.7 V. In the first discharge process, specific capacities of 515.8, 492.9 and 446.1 $mAh \, g^{-1}$ are delivered for $FeS_2/LS-Na_3SbS_{3.75}Se_{0.25}/Na$, $FeS_2/L-Na_3SbS_{3.75}Se_{0.25}/Na$ and $FeS_2/S-Na_3SbS_{3.75}Se_{0.25}/Na$ cells, respectively. The larger discharge capacity than the theoretical specific capacity of FeS_2 (445 $mAh \, g^{-1}$) might be caused by the formation of sodium-solid electrolyte interface in the first cycle [30]. The first Coulombic efficiency of $FeS_2/LS-Na_3SbS_{3.75}Se_{0.25}/Na$ battery is 80.4%, which is higher than those of $FeS_2/L-Na_3SbS_{3.75}Se_{0.25}/Na$ (75.7%) and $FeS_2/S-Na_3SbS_{3.75}Se_{0.25}/Na$ (64.2%)
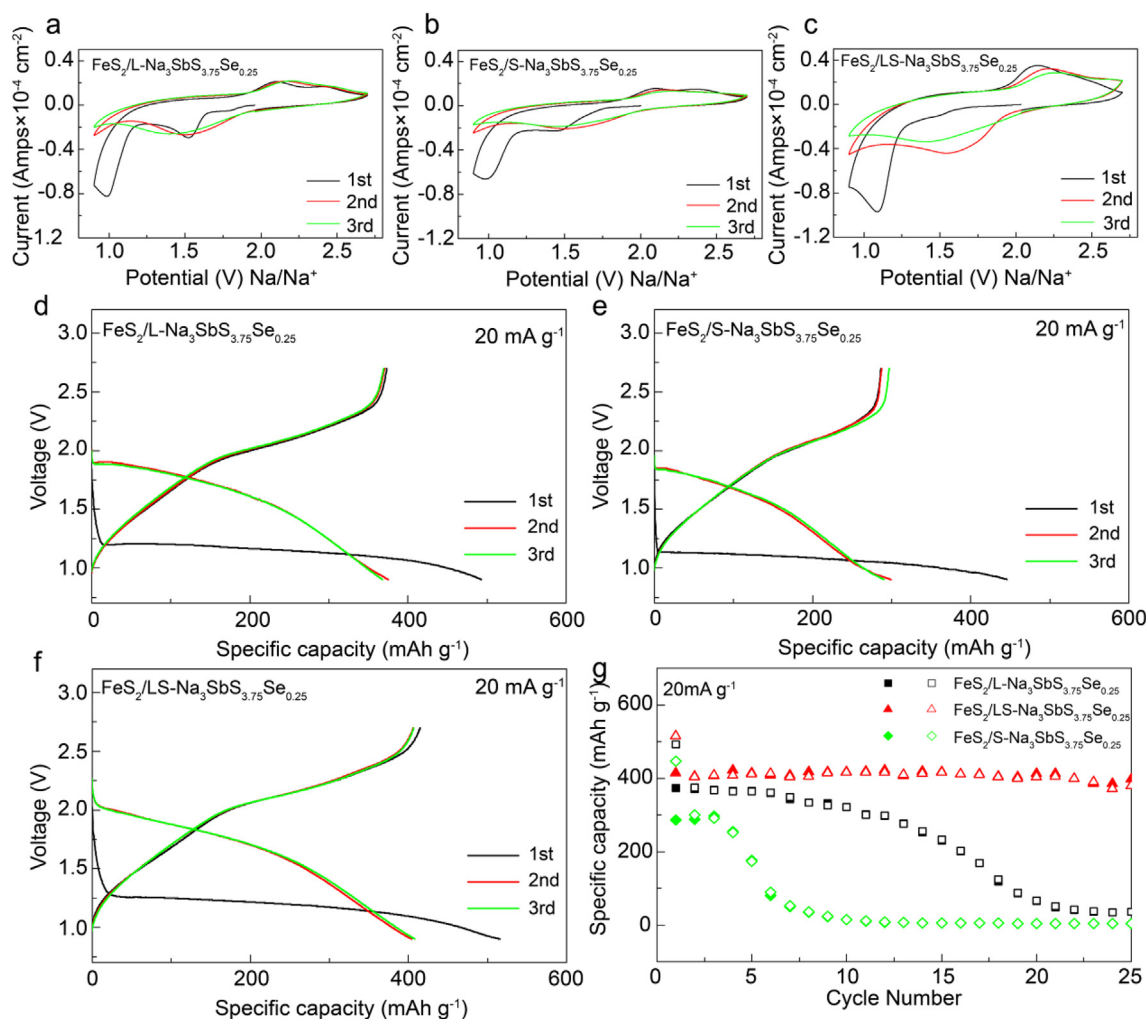
Fig. 4. Cyclic voltammogram for (a) FeS_2/L-$Na_3SbS_{3.75}Se_{0.25}$/Na battery, (b) FeS_2/S-$Na_3SbS_{3.75}Se_{0.25}$/Na battery and (c) FeS_2/LS-$Na_3SbS_{3.75}Se_{0.25}$/Na battery. Galvanostatic discharge/charge profiles of (d) FeS_2/L-$Na_3SbS_{3.75}Se_{0.25}$/Na battery, (e) FeS_2/S-$Na_3SbS_{3.75}Se_{0.25}$/Na battery and (f) FeS_2/LS-$Na_3SbS_{3.75}Se_{0.25}$/Na battery at a current density of $20\,mA\,g^{-1}$. (g) Cycling performance of FeS_2/$Na_3SbS_{3.75}Se_{0.25}$/Na batteries at a current density of $20\,mA\,g^{-1}$.

cells. The improved Coulombic efficiency is attributed to the enhanced interfacial contact in FeS_2/LS-$Na_3SbS_{3.75}Se_{0.25}$/Na cell and high ionic conductivity of LS-$Na_3SbS_{3.75}Se_{0.25}$ electrolyte. The low interface resistance and high ionic conductivity in FeS_2/LS-$Na_3SbS_{3.75}Se_{0.25}$/Na cells also enhances the reversible capacity and cycling stability. Fig. 4g shows the cycling stability of three FeS_2/$Na_3SbS_{3.75}Se_{0.25}$/Na all-solid-state sodium batteries at a current density of $20\,mA\,g^{-1}$. For FeS_2/LS-$Na_3SbS_{3.75}Se_{0.25}$/Na cell, a high specific discharge capacity of 397.2 mAh g^{-1} is still maintained after 25 cycles. By contrast, the discharge capacity of FeS_2/L-$Na_3SbS_{3.75}Se_{0.25}$/Na and FeS_2/S-$Na_3SbS_{3.75}Se_{0.25}$/Na cells decreases rapidly to 36.2 mAh g^{-1} and 3.6 mAh g^{-1} at 25 cycles, respectively.

The rate capability of FeS_2/LS-$Na_3SbS_{3.75}Se_{0.25}$/Na battery was evaluated at different current densities after twenty activation cycles. As shown in Fig. 5a, the FeS_2/LS-$Na_3SbS_{3.75}Se_{0.25}$/Na battery can provide capacities of 365.3, 301.8, 210.1 and 96.0 mAh g^{-1} at 50, 300, 500 and $1000\,mA\,g^{-1}$, respectively. Fig. 5b displays cycling performance of FeS_2/LS-$Na_3SbS_{3.75}Se_{0.25}$/Na battery at different current densities. At 30th cycles, a high reversible discharge specific capacity of 371.1, 319.1, 229.5 and 96.8 mAh g^{-1} is obtained at current densities of 50, 300, 500 and $1000\,mA\,g^{-1}$, respectively. The long cycling stability of the battery was further measured at a high current density of $500\,mA\,g^{-1}$ (Fig. 5c). After 300 cycles, the discharge specific capacity of FeS_2/LS-$Na_3SbS_{3.75}Se_{0.25}$/Na battery still retains at about 140.6 mAh g^{-1}. The superior electrochemical performance in terms of high

capacity, excellent high rate capability and extraordinary cycling stability at different current densities attributes to the following two aspects: First, the high ionic conductivity of LS-$Na_3SbS_{3.75}Se_{0.25}$ electrolyte synthesized by liquid/solid fusion technology improve the electrochemical kinetic process, which will benefit the rate capability and cycling performance under high current density. Second, the large contact area between electrode material and electrolyte due to the reduced particle size further reduces the interface resistance.

4. Conclusion

In summary, tetragonal phase LS-$Na_3SbS_{3.75}Se_{0.25}$ electrolyte with particle size of 200–500 nm and high ionic conductivity of $4.03 \times 10^{-3}\,S\,cm^{-1}$ was successfully synthesized using a liquid/solid fusion technology. Benefited from the intimate solid-solid contact and superior high ionic conductivity of the LS-$Na_3SbS_{3.75}Se_{0.25}$ electrolytes, all-solid-state FeS_2/LS-$Na_3SbS_{3.75}Se_{0.25}$/Na battery shows an excellent rate capability of 365.3, 301.8, 210.1 and 96.0 mAh g^{-1}, at current densities of 50, 300, 500 and $1000\,mA\,g^{-1}$, respectively, and long cycling stability by maintaining a high capacity of 140.6 mAh g^{-1} at a high current density of $500\,mA\,g^{-1}$ for 300 cycles.
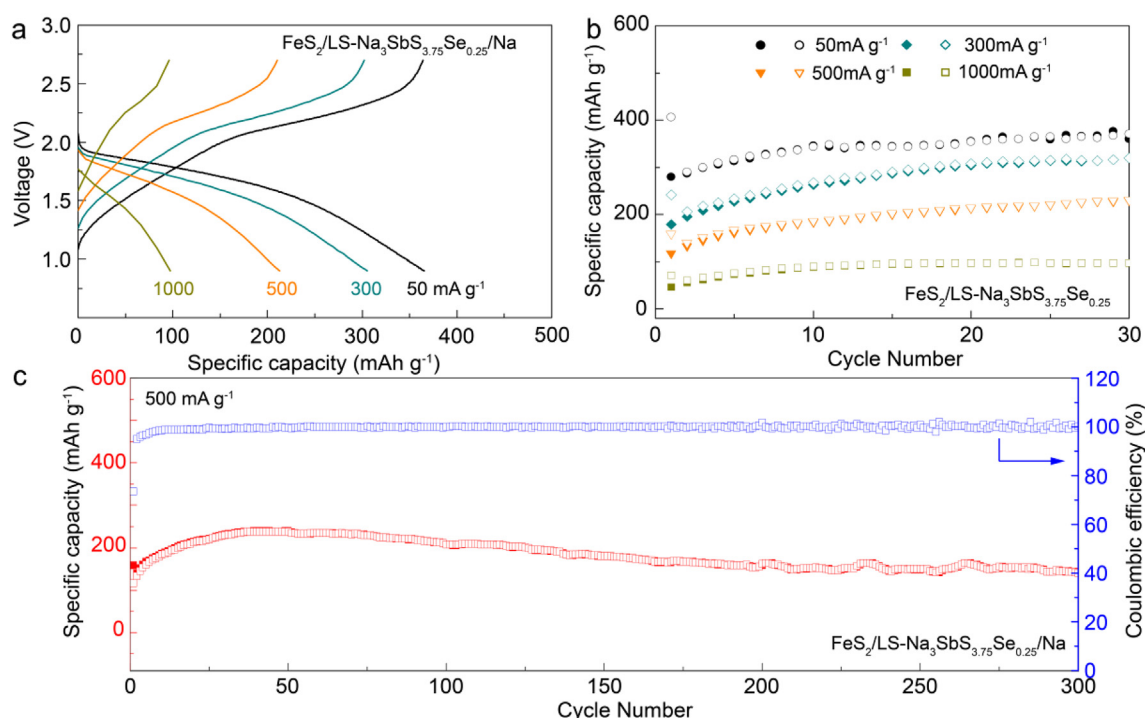
Fig. 5. (a) High rate capability and (b) cycling performance of FeS_2/LS-$Na_3SbS_{3.75}Se_{0.25}$/Na battery under different current densities. (c) High rate cycling stability of the battery at a current density of $500\,mA\,g^{-1}$.

References

[1] Z.W. Seh, J. Sun, Y. Sun, Y. Cui, ACS Cent. Sci. 1 (2015) 449–455.
[2] S. Choudhury, S. Wei, Y. Ozhabes, D. Gunceler, M.J. Zachman, Z. Tu, J.H. Shin, P. Nath, A. Agrawal, L.F. Kourkoutis, T.A. Arias, L.A. Archer, Nat. Commun. 8 (2017) 898.
[3] A. Banerjee, K.H. Park, J.W. Heo, Y.J. Nam, C.K. Moon, S.M. Oh, S.T. Hong, Y.S. Jung, Angew. Chem. Int. Ed. 55 (2016) 9634–9638.
[4] X.W. Chi, Y.L. Liang, F. Hao, Y. Zhang, J. Whiteley, H. Dong, P. Hu, S. Lee, Y. Yao, Angew. Chem. Int. Ed. 57 (2018) 2630–2634.
[5] I.H. Chu, C.S. Kompella, H. Nguyen, Z. Zhu, S. Hy, Z. Deng, Y.S. Meng, S.P. Ong, Sci. Rep. 6 (2016) 33733.
[6] X.L. Fan, J. Yue, F.D. Han, J. Chen, T. Deng, X.Q. Zhou, S. Hou, C.S. Wang, ACS Nano 12 (2018) 3360–3368.
[7] J. Yue, F.D. Han, X.L. Fan, X.Y. Zhu, Z.H. Ma, J. Yang, C.S. Wang, ACS Nano 11 (2017) 4885–4891.
[8] K. Vignarooban, R. Kushagra, A. Elango, P. Badami, B.E. Mellander, X. Xu, T.G. Tucker, C. Nam, A.M. Kannan, Int. J. Hydrogen Energy 41 (2016) 2829–2846.
[9] C.L. Zhao, L.L. Liu, X.G. Qi, Y.X. Lu, F.X. Wu, J.M. Zhao, Y. Yu, Y.-S. Hu, L.Q. Chen, Adv. Energy Mater. 8 (2018) 1703012.
[10] J.-K. Kim, Y.J. Lim, H. Kim, G.-B. Cho, Y. Kim, Energy Environ. Sci. 8 (2015) 3589–3596.
[11] Z.Z. Zhang, Q.Q. Zhang, C. Ren, F. Luo, Q. Ma, Y.-S. Hu, Z.B. Zhou, H. Li, X.J. Huang, L.Q. Chen, J. Mater. Chem. A 4 (2016) 15823–15828.
[12] A. Hayashi, K. Noi, A. Sakuda, M. Tatsumisago, Nat. Commun. 3 (2012) 856.
[13] H. Wang, Y. Chen, Z.D. Hood, G. Sahu, A.S. Pandian, J.K. Keum, K. An, C. Liang, Angew. Chem. Int. Ed. 55 (2016) 8551–8555.
[14] L. Zhang, K. Yang, J.L. Mi, L. Lu, L.R. Zhao, L.M. Wang, Y.M. Li, H. Zeng, Adv. Energy Mater. 5 (2015) 1501294.
[15] Z.X. Yu, S.-L. Shang, Y. Gao, D.W. Wang, X.L. Li, Z.-K. Liu, D.H. Wang, Nano Energy 47 (2018) 325–330.
[16] H.L. Wan, J.P. Mwizerwa, X.G. Qi, X. Liu, X.X. Xu, H. Li, Y.-S. Hu, X.Y. Yao, ACS Nano 12 (2018) 2809–2817.
[17] H.L. Wan, J.P. Mwizerwa, X.G. Qi, X.X. Xu, H. Li, Q. Zhang, L.T. Cai, Y.-S. Hu, X.Y. Yao, ACS Appl. Mater. Interfaces 10 (2018) 12300–12304.
[18] W. Hou, X. Guo, X. Shen, K. Amine, H. Yu, J. Lu, Nano Energy 52 (2018) 279–291.
[19] N. Tanibata, K. Noi, A. Hayashi, M. Tatsumisago, RSC Adv. 4 (2014) 17120–17123.
[20] Z. Zhang, E. Ramos, F. Lalère, A. Assoud, K. Kaup, P. Hartman, L.F. Nazar, Energy Environ. Sci. 11 (2018) 87–93.
[21] X.Y. Yao, D. Liu, C.S. Wang, P. Long, G. Peng, Y.-S. Hu, H. Li, L.Q. Chen, X.X. Xu, Nano Lett. 16 (2016) 7148–7154.
[22] J.M. Whiteley, S. Hafner, S.S. Han, S.C. Kim, K.H. Oh, S.-H. Lee, Adv. Energy Mater. 6 (2016) 1600495.
[23] Z. Liu, W. Fu, E.A. Payzant, X. Yu, Z. Wu, N.J. Dudney, J. Kiggans, K. Hong, A.J. Rondinone, C. Liang, J. Am. Chem. Soc. 135 (2013) 975–978.
[24] Z.D. Hood, H. Wang, A.S. Pandian, R. Peng, K.D. Gilroy, M. Chi, C. Liang, Y. Xia, Adv. Energy Mater. (2018) 1800014.
[25] L. Zhang, D.C. Zhang, K. Yang, X.L. Yan, L.M. Wang, J.L. Mi, B. Xu, Y.M. Li, Adv. Sci. 3 (2016) 1600089.
[26] P. Bron, S. Johansson, K. Zick, J. Schmedt auf der Gunne, S. Dehnen, B. Roling, J. Am. Chem. Soc. 135 (2013) 15694–15697.
[27] S. Ito, M. Nakakita, Y. Aihara, T. Uehara, N. Machida, J. Power Sources 271 (2014) 342–345.
[28] Y.Y. Chen, X.D. Hu, B. Evanko, X.H. Sun, X. Li, T.Y. Hou, S. Cai, C.M. Zheng, W.B. Hu, G.D. Stucky, Nano Energy 46 (2018) 117–127.
[29] Z. Hu, Z. Zhu, F. Cheng, K. Zhang, J. Wang, C. Chen, J. Chen, Energy Environ. Sci. 8 (2015) 1309–1316.
[30] E.A. Wu, C.S. Kompella, Z. Zhu, J.Z. Lee, S.C. Lee, I.H. Chu, H. Nguyen, S.P. Ong, A. Banerjee, Y.S. Meng, ACS Appl. Mater. Interfaces 10 (2018) 10076–10086.

Hongli Wan is pursuing her Ph.D. degree at Ningbo Institute of Materials Technology and Engineering, Chinese Academy of Sciences. She is currently a joint Ph.D. student at Department of Chemical and Biomolecular Engineering, University of Maryland-College Park. Her research focuses on transitional metal sulfide based all-solid-state batteries.

Jean Pierre Mwizerwa received his bachelor's degree in chemistry with education at University of Rwanda and his master's degree in physical chemistry at Xiamen University, P. R. China. His research focuses on energy storage and conversion materials. Currently, he is pursuing Ph.D. degree at Ningbo Institute of Materials Technology and Engineering, Chinese Academy of Sciences. He is conducting research on sulfide cathode materials for all-solid-state lithium batteries.

Jing Yang received his Ph.D. degree in materials science and engineering at Wuhan University of Technology in 2017. Now, he is a post-doctoral researcher in Ningbo Institute of Materials Technology and Engineering, Chinese Academy of Sciences. His research focuses on the lithium/sodium solid electrolytes and all-solid-state rechargeable batteries.
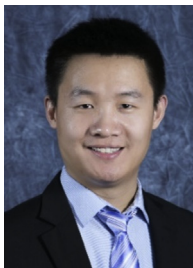
Fudong Han is currently an Assistant Professor and Priti and Mukesh Chatter '82 Career Development Chair at Rensselaer Polytechnic Institute. He received his BS degree in 2009 and his MS degree in 2012 in Materials Science and Engineering from Shandong University, and his PhD degree in Chemical Engineering from the University of Maryland College Park in 2018. His research focuses on materials for electrochemical energy storage with a special focus on all-solid-state batteries. He is the recipient of a 2017 MRS Graduate Student Gold Award and 2018 ECS Battery Division Student Research Award.

Chunsheng Wang is a Robert Franklin and Frances Riggs Wright Distinguished Chair Professor at the University of Maryland-College Park. He is an associate editor of *ACS Applied Energy Materials*, and UMD Director of Center for Research in Extreme Batteries. He has published more than 230 papers including Science, Nature, Nature Materials, Nature Nanotechnology, and Nature Communications. His work has been cited for more than 20000 times with H-index of 73. Dr. Wang is the recipient of the Junior Faculty Outstanding Research Award in the University of Maryland in 2013, and winner of UMD's invention of the Year for 2015.

Wei Weng received his bachelor's degree in material physics at Wuhan University of Technology in 2017. Now, he is pursuing his Ph.D. degree at Ningbo Institute of Materials Technology and Engineering, Chinese Academy of Sciences. His research focuses on solid electrolyte materials for all-solid-state batteries.

Xiayin Yao is a professor at Ningbo Institute of Materials Technology and Engineering, Chinese Academy of Sciences (NIMTE, CAS). He received Ph.D from Institute of Solid State Physics and NIMTE, CAS in 2009. After that, he joined NIMTE and worked there until now. During 2012–2014, he was a research fellow in Hanyang University, S. Korea and Nanyang Technological University, Singapore. So far, he has coauthored over 90 peer-reviewed journal papers and applied more than 30 Chinese patents. His major interests include developing solid state electrolytes with high ionic conductivities and solid-state lithium-sulfur batteries as well as solid-state sodium batteries.